

Coherence of resonant-tunneling transport in terahertz quantum-cascade lasers

Sushil Kumar and Qing Hu

*Department of Electrical Engineering and Computer Science and Research Laboratory of Electronics,
Massachusetts Institute of Technology, Cambridge, Massachusetts 02139, USA*

(Received 23 July 2009; revised manuscript received 6 October 2009; published 15 December 2009)

We develop simple density-matrix models to describe the role of coherence in resonant-tunneling (RT) transport of quantum-cascade lasers (QCLs). Specifically, we investigate the effects of coherent coupling between the lasing levels with other levels on the transport properties and gain spectra. In the first part of the paper, we use a three-level density-matrix model to obtain useful analytical expressions for current transport through the injector barrier in a QCL. An expression for the slope discontinuity in the current-voltage characteristics at the lasing threshold is derived. This value is shown to be a direct measure of the population inversion at threshold and contradicts the previously held belief of it being indicative of ratio of the laser level lifetimes. In the second part of the paper, we use density matrices to compute the gain spectrum for a resonant-phonon terahertz QCL design. The large anticrossing of the doublet of lower radiative levels is reflected in a broad gain linewidth due to a coherent RT assisted depopulation process. At certain bias conditions, the gain spectrum exhibits double peaks which is supported by experimental observations.

DOI: [10.1103/PhysRevB.80.245316](https://doi.org/10.1103/PhysRevB.80.245316)

PACS number(s): 73.63.-b, 78.67.Pt, 05.60.Gg, 42.55.Px

I. INTRODUCTION

The role of sequential resonant tunneling (RT) in semiconductor quantum wells for charge transport¹ as well as light amplification² has been discussed since the early 1970s. Subsequently, multiple proposals were introduced in the 1980s to predict intersubband lasing in semiconductor superlattice structures. With the advent of a unique RT based charge injection scheme, a unipolar mid-infrared (IR) intersubband laser, the so-called quantum-cascade laser (QCL), was first demonstrated in 1994.³ Mid-IR QCLs have since undergone rapid progress and room-temperature continuous-wave (cw) operation is now obtained over the $\lambda \sim 4\text{--}10\ \mu\text{m}$ spectrum. Based on similar design principles, the operating frequency range of these devices has also been extended to terahertz frequencies ($\nu \sim 1\text{--}5\ \text{THz}$ and $\lambda \sim 60\text{--}300\ \mu\text{m}$).⁴ However, due to additional challenges associated with the charge transport in these low-frequency devices, terahertz QCLs are still required to be cryogenically cooled.⁵⁻⁷ It then becomes increasingly important to better understand the transport processes in terahertz QCLs to improve the existing designs, with a goal to ultimately achieve room-temperature operation.

The best temperature performance for terahertz QCLs is obtained with the resonant-phonon (RP) designs,^{8,9} and operation up to 186 K without magnetic field¹⁰ and 225 K with magnetic field¹¹ has been demonstrated. For QCLs, almost universally across all different designs and operating frequencies, RT plays an important role in the electrical injection process to populate the upper radiative level.^{12,13} For the resonant-phonon terahertz QCLs (RPTQCLs), RT also plays an important role in the lower-level depopulation. Newer designs with RT based extraction have also been demonstrated recently achieving very low threshold current densities.^{14,15} The radiative levels in a terahertz QCL have small energy separation in the range of $\hbar\omega \sim 4\text{--}20\ \text{meV}$ ($\nu \sim 1\text{--}5\ \text{THz}$). The potential barriers in the multiple quantum-well (QW) structure are therefore kept thick to obtain tightly coupled

levels in order to maintain selectivity of the injection as well as the depopulation processes. This makes the coupling energies (as characterized by the anticrossing energy $2\hbar\Omega_{ij}$ for the coupled levels i and j) similar in value to the low-temperature energy-level broadening, which is expected to be on the order of a few millielectronvolt. Consequently, the loss of coherence (or dephasing) in the RT process has a significant bearing on the electron transport across the barriers.¹⁶

In this paper, simple density-matrix (DM) models are used to incorporate the important role of coherence in the RT transport of QCLs. We consider the case of tight binding for intermodule transport since the intermodule energy anticrossings $2\hbar\Omega_{ij}$ are typically much smaller than the intramodule energy-level separations, where each module can consist of one or more QWs and the QCL structure is a periodic repetition of one or more such modules. In the first part of the paper, we use a density-matrix model similar to the two-level model first proposed by Kazarinov and Suris¹⁷ and then later also discussed in Refs. 12, 18, and 19 among others. We modify the model to extend to three levels to describe a QCL in a more general sense and derive analytical expressions for current transport across the injector barrier both below and above the lasing threshold. Despite the simplicity of the model, we can gain useful information about QCL operation from the derived results that includes information about the possible temperature degradation mechanisms in RPTQCLs. The results presented in this section are applicable to mid-IR QCLs as well. In the second part of the paper, we use a similar model to estimate the optical gain spectrum of RPTQCLs. A coherent RT assisted depopulation process is stipulated to be the cause of broad gain bandwidths that are typically observed in these lasers.²⁰

II. CURRENT TRANSPORT IN A THREE-LEVEL QCL

An accurate estimation of the electrical transport characteristics of a QCL is quite challenging and more so for a

terahertz QCL. Computationally intensive numerical techniques based on Monte Carlo simulations¹⁶ and nonequilibrium Green's functions²¹ have produced reasonably good results; however, an accurate description of the temperature degradation mechanisms in terahertz QCLs is still lacking. Also, such computational techniques fall short of providing a good intuitive picture of QCL operation. Hence, more often than not, analysis based on simple rate equations are used during the design process. The three-level model presented in this section is a step toward developing a simpler transport model that still captures the nuances of QCL operation and also provides a better understanding of how various parameters affect its characteristics both below and above the lasing threshold.

For simplicity yet still captures the essentials, in what follows we discuss a three-level QCL design with two wells per module as shown in Fig. 1 (Refs. 22 and 23) in which level 1' is the injector state and the radiative transition is from level 3 \rightarrow 2. Even though typically QCL designs include many more levels per period, the results obtained here hold for the triplet of levels consisting of the injector level and the two radiative levels [levels 1', 3, and 2 in Fig. 1(b)], regardless of a particular design, and including the mid-IR designs. Due to the various intrasubband and intersubband scattering mechanisms that contribute to quantum transport, the electron wave packets undergo dephasing, which manifests itself as broadening of the energy levels. The tunnel coupling between the levels of the same module is strong, therefore, dephasing has a relatively negligible effect on the intramodule intersubband transport.¹⁶ However, the intermodule transport across the injector barrier is critically affected by the dephasing time of the wave packets since the 1' \rightarrow 3 tunneling time (half of the interwell Rabi oscillation period $\pi/\Omega_{1'3}$) is now longer and of the same order. To incorporate the role of coherence in the 1' \rightarrow 3 RT transport, we use DM rate equations corresponding to the tight-binding basis states of Fig. 1(b).¹⁶ The time evolution of the 3×3 DM for this basis set can be written as²²

$$\frac{d}{dt} \bar{\rho}_{(1',3,2)} = -\frac{i}{\hbar} [\bar{H}_{\text{ext}}, \bar{\rho}_{(1',3,2)}] - \frac{i}{\hbar} [\bar{H}', \bar{\rho}_{(1',3,2)}], \quad (1)$$

where \bar{H}' includes various radiative and nonradiative perturbation potentials to the conduction-band potential \bar{H}_{ext} . The advantage of writing the DMs with the tight-binding basis of Fig. 1(b) is twofold. First, it allows inclusion of dephasing

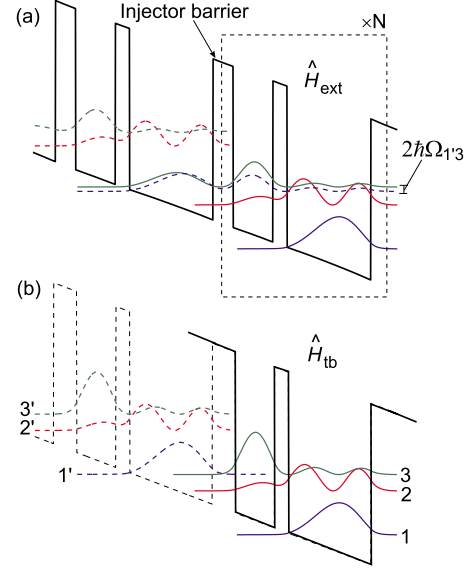


FIG. 1. (Color online) Plot of the magnitude squared envelope wave functions for a three-level QCL design with two different sets of basis functions. Plot (a) is for the “extended” scheme, where energy splitting due to the injector anticrossing $2\hbar\Omega_{1'3}$ is visible and the wave functions are calculated for a potential profile \hat{H}_{ext} as it appears in the figure. Plot (b) is for the “tight-binding” scheme, where the potential \hat{H}_{tb} is formed by making the barriers at the boundaries of a module sufficiently thick to confine the wave functions within the module.

phenomenologically by means of decay of the coherences associated with levels 1' and 3 due to nonzero off-diagonal terms in \bar{H}_{ext} corresponding to those levels. Second, whereas the eigenstates of \hat{H}_{ext} depend sensitively on the externally applied electrical bias because of coupling between spatially separated states, the chosen basis states remain more or less independent of the bias in the range of interest (i.e., close to the “design bias” corresponding to the 1'-3 alignment), which keeps the form factors for various intramodule scattering rate calculations approximately invariant of bias. In a first-order approximation, we assume RT to be independent of the electron wave vector in the plane of the QWs. The subband lifetimes are assumed to be averaged over the electron distribution within a subband and are to be calculated within the Fermi's golden rule approximation. Expanding Eq. (1), we then obtain

$$\frac{d}{dt} \bar{\rho}_{(1',3,2)} = -i \left[\begin{pmatrix} E_1/\hbar & -\Omega_{1'3} & -\Omega_{1'2} \\ -\Omega_{1'3} & E_3/\hbar & 0 \\ -\Omega_{1'2} & 0 & E_2/\hbar \end{pmatrix}, \bar{\rho}_{(1',3,2)} \right] + \begin{pmatrix} \frac{\rho_{33} + \rho_{22}}{\tau_{31} \tau_{21}} & -\frac{\rho_{1'3}}{\tau_{\parallel 13}} & -\frac{\rho_{1'2}}{\tau_{\parallel 12}} \\ -\frac{\rho_{31'}}{\tau_{\parallel 13}} & -\frac{\rho_{33}}{\tau_3} - \frac{\rho_{33} - \rho_{22}}{\tau_{\text{st}}} & -\frac{\rho_{32}}{\tau_{\parallel 23}} \\ -\frac{\rho_{21'}}{\tau_{\parallel 12}} & -\frac{\rho_{23}}{\tau_{\parallel 23}} & \frac{\rho_{33}}{\tau_{32}} + \frac{\rho_{33} - \rho_{22}}{\tau_{\text{st}}} - \frac{\rho_{22}}{\tau_{21}} \end{pmatrix}. \quad (2)$$

In the equation above

$$\bar{\rho}_{(1',3,2)} \equiv \begin{pmatrix} \rho_{1'1'} & \rho_{1'3} & \rho_{1'2} \\ \rho_{31'} & \rho_{33} & \rho_{32} \\ \rho_{21'} & \rho_{23} & \rho_{22} \end{pmatrix},$$

where $\rho_{ii} (=n_i)$ is taken as the number of electrons per module in level i and ρ_{ij} is the coherence (also known as polarization) term for levels i, j . In \hat{H}_{ext} , the diagonal terms are the level energies given by $\hat{H}_{nn} = \langle n | \hat{H}_{\text{ext}} | n \rangle \approx E_n$ and the level anticrossings are represented in the off-diagonal terms as $\hat{H}_{mn} = \langle m | \hat{H}_{\text{ext}} - \hat{H}_{\text{tb}} | n \rangle \approx -\hbar \Omega_{mn}$. For the lifetimes, τ_{ij} is the intersubband scattering time from $i \rightarrow j$, $\frac{1}{\tau_{ij}} \equiv \frac{1}{2\tau_i} + \frac{1}{2\tau_j} + \frac{1}{T_2^*}$ is the dephasing rate for the coherence term ρ_{ij} that consists of lifetime broadening terms as well as a phenomenological broadening term T_2^* due to interface roughness and impurity scattering¹⁶ and τ_{st} is due to the radiative stimulated emission above the lasing threshold ($\rightarrow \infty$ below threshold). The back-scattering times τ_{23} and τ_{12} can also be included in Eq. (2) if relevant for a particular design. Note that $\Omega_{32} = 0$ for the chosen bases since subbands 3 and 2 are the eigenstates of the tight-binding potential \hat{H}_{tb} in Fig. 1(b). By such a choice, the role of coherence in $3 \rightarrow 2$ transport cannot be included. This does not introduce a large error in estimating the current flow since 3 and 2 are strongly coupled. In other words, if tight-binding bases were chosen for the radiative subbands 3 and 2 across the middle “radiative” barrier of the two-well module, Ω_{32} would be large and the Rabi oscillation period π/Ω_{32} would be much smaller than the dephasing time $\tau_{\parallel 32}$ for the $3 \rightarrow 2$ tunneling, making $\tau_{\parallel 32}$ inconsequential for the $3 \rightarrow 2$ transport.

As a simpler alternative to more advanced methods, Eq. (2) can model some aspects of QCL transport fairly accu-

ately. Although it could be solved numerically, we seek analytical expressions that could provide a greater understanding about the effect of various parameters on the transport. Toward that goal, we assume $\Omega_{1'2} \approx 0$ akin to a unity $1' \rightarrow 3$ injection selectivity. This assumption is, in general, valid for mid-IR designs due to a large radiative level separation $E_{32} (=E_3 - E_2)$ and also becomes reasonable for the diagonal terahertz designs.¹⁰ Within this approximation, Eq. (2) can be reduced to that with 2×2 matrices as follows:

$$\frac{d}{dt} \bar{\rho}_{(1',3)} = -i \left[\begin{pmatrix} E_{1'}/\hbar & -\Omega_{1'3} \\ -\Omega_{1'3} & E_3/\hbar \end{pmatrix}, \bar{\rho}_{(1',3)} \right] + \begin{pmatrix} \rho_{33} + \frac{\rho_{22}}{\tau_{31}} & -\frac{\rho_{1'3}}{\tau_{\parallel}} \\ \frac{-\rho_{31'}}{\tau_{\parallel}} & -\frac{\rho_{33}}{\tau_{31}} - \frac{\rho_{22}}{\tau_{21}} \end{pmatrix}, \quad (3)$$

where $\bar{\rho}_{(1',3)} \equiv \begin{pmatrix} \rho_{1'1'} & \rho_{1'3} \\ \rho_{31'} & \rho_{33} \end{pmatrix}$, $\tau_{\parallel} \equiv \tau_{\parallel 13}$, $\tau_3 \equiv \frac{\tau_{31}\tau_{32}}{\tau_{31} + \tau_{32}}$, and $\frac{\rho_{33}}{\tau_3} + \frac{\rho_{33} - \rho_{22}}{\tau_{\text{st}}}$ from Eq. (2) is substituted by $\frac{\rho_{33}}{\tau_{31}} + \frac{\rho_{22}}{\tau_{21}}$ in Eq. (3), which holds when $\Omega_{1'2} = 0$ as a statement of current continuity. Additionally, we can write the following equation for ρ_{22} below and above the lasing threshold:

$$\rho_{22} = \begin{cases} \rho_{33} \frac{\tau_{21}}{\tau_{32}} & \cdots (I < I_{\text{th}}), \\ \rho_{33} - \Delta n_{\text{th}} & \cdots (I \geq I_{\text{th}}), \end{cases} \quad (4)$$

where $\Delta n_{\text{th}} = (\rho_{33} - \rho_{22})_{\text{th}}$ is the population inversion at threshold that is assumed to remain constant beyond threshold. Equations (3) and (4) can be solved analytically for steady state ($\frac{d}{dt} \rightarrow 0$). With the constraint $n_{\text{tot}} = (\rho_{11} + \rho_{22} + \rho_{33})$, where n_{tot} is the total number of electrons per module and is a constant, the following expressions are obtained for the current I (Ref. 22):

$$I \equiv |e| \left(\frac{\rho_{33}}{\tau_{31}} + \frac{\rho_{22}}{\tau_{21}} \right) = \begin{cases} |e| n_{\text{tot}} \left[\frac{2\Omega_{1'3}^2 \tau_{\parallel}}{4\Omega_{1'3}^2 \tau_{\parallel} \left(\frac{\tau_{31}\tau_{32}}{\tau_{31} + \tau_{32}} \right) \left(1 + \frac{\tau_{21}}{2\tau_{32}} \right) + \Delta_{1'3}^2 \tau_{\parallel}^2 + 1} \right] & \cdots (I < I_{\text{th}}), \\ |e| n_{\text{tot}} \left[\frac{2\Omega_{1'3}^2 \tau_{\parallel} \left(1 - \frac{2\Delta n_{\text{th}}}{n_{\text{tot}}} \left[\frac{1 - \tau_{21}/(2\tau_{31})}{1 + \tau_{21}/\tau_{31}} \right] \right)}{6\Omega_{1'3}^2 \tau_{\parallel} \left(\frac{\tau_{31}\tau_{21}}{\tau_{31} + \tau_{21}} \right) + \Delta_{1'3}^2 \tau_{\parallel}^2 + 1} \right] & \cdots (I \geq I_{\text{th}}), \end{cases} \quad (5)$$

where e is the unit charge and $\hbar \Delta_{1'3} \equiv E_{1'} - E_3$ is the energy detuning between levels $1'$ and 3 that is a function of the externally applied electrical bias. For the case of ultrashort lifetime of the lower radiative state ($\tau_{21} \ll 2\tau_{32}$), the below-threshold term in Eq. (5) becomes

$$I = \frac{|e| n_{\text{tot}}}{2\tau_3} \left(\frac{4\Omega_{1'3}^2 \tau_{\parallel} \tau_3}{4\Omega_{1'3}^2 \tau_{\parallel} \tau_3 + \Delta_{1'3}^2 \tau_{\parallel}^2 + 1} \right) \cdots (\tau_{21} \ll 2\tau_{32}, I < I_{\text{th}}), \quad (6)$$

which reproduces the commonly used expression in literature.^{2,12}

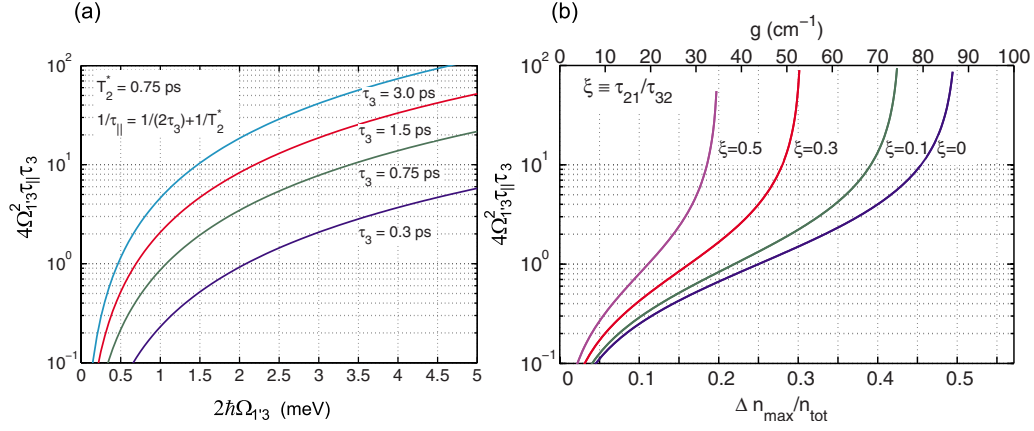


FIG. 2. (Color online) (a) A plot of the factor $4\Omega_{1'3}^2 \tau_{||} \tau_3$ to determine the regime of RT transport through the injector barrier ($\gg 1$ coherent and $\ll 1$ incoherent). A phenomenological value of $T_2^* = 0.75$ ps is assumed. (b) A related plot to determine the maximum value of population inversion ($n_3 - n_2$) that can be attained for a given $\Omega_{1'3}$, calculated using Eq. (10). The top axis converts Δn on the bottom axis to corresponding values of peak gain for the following typical parameters: $n_{tot}/\text{volume} = 5 \times 10^{15}$ cm $^{-3}$, $f_{32} = 0.5$, $\Delta\nu = 1.0$ THz, and using the expression $g \approx 70 \frac{[\Delta n / (10^{15} \text{ cm}^{-3})] f_{32}}{[\Delta\nu / (1 \text{ THz})]}$ [cm $^{-1}$] for GaAs material (Ref. 6) that assumes a Lorentzian gain linewidth of $\Delta\nu$ (note that f_{32} is the oscillator strength of the radiative transition).

Since $\tau_{21} \ll 2\tau_{32}$ typically holds for a QCL design, the below-threshold term for the three-level model in Eq. (5) does not provide any new insight from Eq. (6). However, the advantage of the model lies in describing transport above threshold. It is instructive to write expressions for maximum current (I_{max}), which flows at the $1'-3$ resonance ($\Delta_{1'3} = 0$) for the case of a coherent RT process, i.e., a large injector coupling $\Omega_{1'3}$.^{12,24} The following expressions are obtained for I_{max} and the level populations when threshold could not be attained:

$$I_{max} = \frac{|e|n_{tot}}{2\tau_3 \left(1 + \frac{\tau_{21}}{2\tau_{32}}\right)},$$

$$n_3 = n_1 = n_{tot} \left(\frac{1}{2 + \frac{\tau_{21}}{\tau_{32}}} \right),$$

$$\Delta n \equiv n_3 - n_2 = n_{tot} \left(\frac{1 - \frac{\tau_{21}}{\tau_{32}}}{2 + \frac{\tau_{21}}{\tau_{32}}} \right) \cdots (4\Omega_{1'3}^2 \tau_{||} \tau_3 \gg 1, \quad I_{max} < I_{th}).$$

(7)

The results in Eq. (7) are slightly different than that obtained using a two-level model in Ref. 12 as a consequence of adding an additional level (i.e., the lower laser subband 2) in these calculations. However, the commonly used two-level model result $I_{max} = |e|n_{tot}/(2\tau_3)$ is recovered in the limit $\tau_{21} \ll \tau_{32}$ as it is to be expected. Equation (7) suggests that I_{max} for coherent injection is independent of $\Omega_{1'3}$, and therefore the thickness of the injector barrier, and is limited by the upper-state lifetime τ_3 . Typical values of $\Omega_{1'3}$ that bring a

QCL within this limit could be determined from Fig. 2(a). The value of I_{max} , however, is different if enough population inversion could be attained prior to the $1'-3$ resonance and the device starts lasing in which case stimulated emission lowers the upper-state lifetime. In such a scenario, the maximum current is limited by the lower-state lifetime τ_{21} instead and is given by

$$I_{max} = \frac{|e|n_{tot}}{3\tau_{21}} \left[1 - \frac{2\Delta n_{th}}{n_{tot}} + \frac{\tau_{21}}{\tau_{31}} \left(1 + \frac{\Delta n_{th}}{n_{tot}} \right) \right],$$

$$n_3 = n_1 = \left(\frac{n_{tot}}{3} + \frac{\Delta n_{th}}{3} \right) \cdots (6\Omega_{1'3}^2 \tau_{||} \tau_{21} \gg 1, \quad I_{max} > I_{th}).$$

(8)

Equation (8) implies that a QCL with a large injector coupling $\Omega_{1'3}$ and a short lower-state lifetime τ_{21} can possibly obtain a large dynamic range in current due to a large I_{max} [see Figs. 3(c) and 3(d)]. However, it may be noted that for coherent injection, the gain linewidth of the QCL becomes additionally broadened as the injector coupling $\Omega_{1'3}$ is increased. Consequently, a larger Δn_{th} is required to attain a certain value of peak gain, which mitigates the increase in the value of I_{max} . This will become more clear in Sec. III from the gain spectrum calculations for some specific cases.

Approaching threshold, the value of current that must flow through the QCL structure to establish a population inversion of Δn_{th} is calculated to be

$$I_{th} = \frac{|e|\Delta n_{th}}{\tau_3 \left(1 - \frac{\tau_{21}}{\tau_{32}} \right)}.$$

(9)

While the above expression for I_{th} can also be derived from a simple rate equation analysis, the minimum value of $\Omega_{1'3}$ needed for a current I_{th} to flow through the structure is derived from the present three-level DM model as

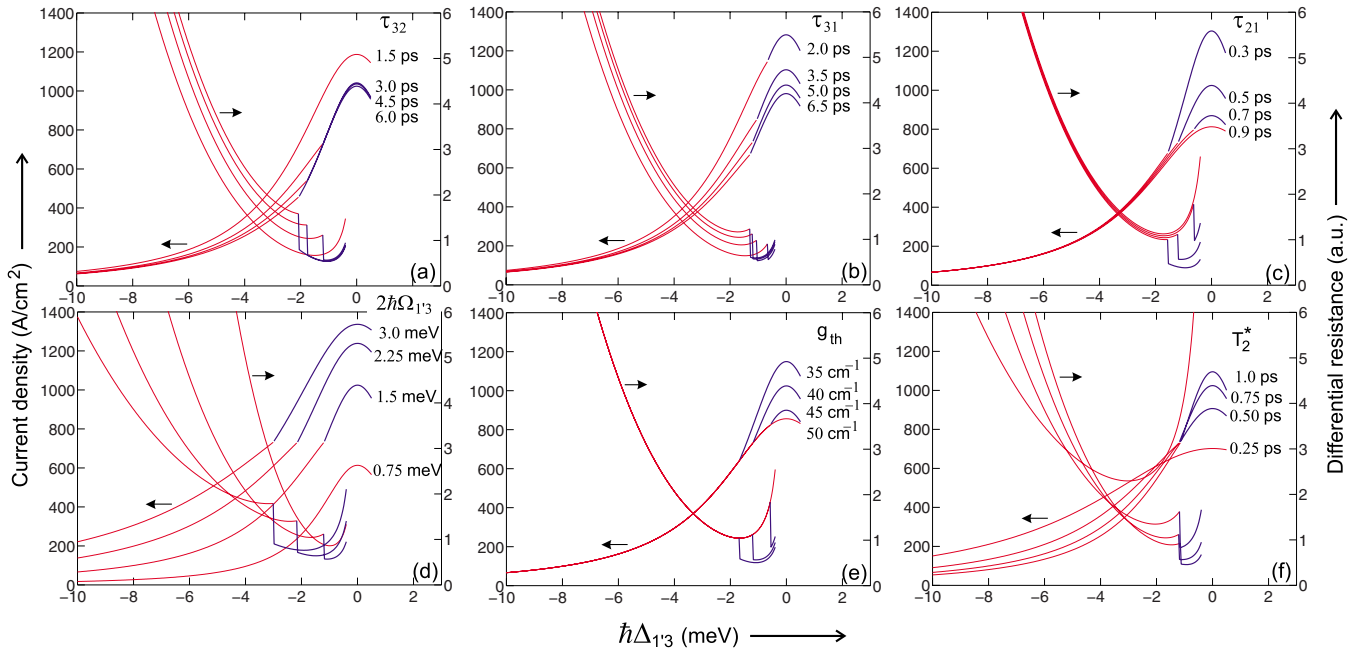


FIG. 3. (Color online) Calculations of the current density (I/area) as a function of the energy detuning $\hbar\Delta_{1'3}$ [which is proportional to the external bias voltage V , as in Eq. (12)] and its inverse slope $\frac{\hbar}{|e|} \frac{d\Delta_{1'3}}{dI}$ [which is proportional to the differential resistance \mathcal{R} , as in Eq. (13)]. The calculations are done for a range of parameters using Eq. (5) for the three-level model. Following default values are chosen corresponding to the typical values for RPTQCL designs: $2\hbar\Omega_{1'3}=1.5$ meV, $T_2^*=0.75$ ps, $g_{\text{th}}=40/\text{cm}$ (Ref. 25), $\tau_{21}=0.5$ ps, $\tau_{32}=3.0$ ps, and $\tau_{31}=5.0$ ps. A doping density $n_{\text{tot}}/\text{volume}=5 \times 10^{15}$ cm^{-3} is used. The radiative transition is assumed to have a Lorentzian linewidth of $\Delta\nu=1.5$ THz (the broad linewidth is based on the findings of Sec. III) and an oscillator strength of $f_{32}=0.6$ to determine the population inversion Δn_{th} required to attain a particular value of threshold gain g_{th} . The thin (red) portion of the curves corresponds to $I < I_{\text{th}}$ while the thick (blue) region is for $I > I_{\text{th}}$ where the occurrence of threshold is marked by a discontinuity in \mathcal{R} . Each of the subplots show the variation in the I - V 's and the \mathcal{R} - V 's when only a single parameter is changed, the others being kept at the values mentioned above. Note that additional linewidth broadening due to coherent effects (discussed in Sec. III) is not considered for calculations of the curves above threshold.

$$4\Omega_{1'3}^2 \tau_{\parallel} \tau_3 > \frac{2\Delta n_{\text{th}}}{n_{\text{tot}} - 2\Delta n_{\text{th}} - (n_{\text{tot}} + \Delta n_{\text{th}}) \frac{\tau_{21}}{\tau_{32}}}. \quad (10)$$

This result is obtained from Eq. (5) as a necessary condition for the two expressions to have the same value for some particular bias $\Delta_{1'3}$. An estimate of the minimum value of $\Omega_{1'3}$ required to meet this condition can be obtained from the plots in Fig. 2(b). Figure 2(b) can also be interpreted in a different way since it determines the maximum value of population inversion that can be attained for a given $\Omega_{1'3}$. For example, in the limit $\tau_{21} \rightarrow 0$, a maximum of $\Delta n = n_{\text{tot}}/2$ can be obtained if $4\Omega_{1'3}^2 \tau_{\parallel} \tau_3 \gg 1$.

A. Current-voltage characteristics for typical parameters

To gauge the effect of various parameters on QCL's performance, Fig. 3 shows calculation of the current-voltage (I - V) and differential-resistance-voltage (\mathcal{R} - V , $\mathcal{R} = \frac{dV}{dI}$) characteristics for a range of parameters using the analytical expressions in Eq. (5). The I - V 's show a discontinuity in slope at the occurrence of the lasing threshold, as was first discussed in detail in Ref. 12. However, any discussion about the differential resistance in the present context is left until later. For the I - V 's the main features to be noted are the values of the threshold current density J_{th} and the maximum

current density J_{max} . In general for any design, the goal is to obtain a larger dynamic range for lasing $J_{\text{max}}/J_{\text{th}}$ while also keeping the value of J_{th} low. A larger dynamic range leads to greater amount of the optical power output and also a higher operating temperature T_{max} . As it is to be expected, the plots show that the laser performance improves by making τ_{31} and τ_{32} larger, and τ_{21} smaller.

We now compare the three-level model I - V 's in Fig. 3 to those experimentally measured for two different RPTQCL designs. Figure 4 shows typical results from a four-level^{10,26,27} and a five-level^{6,8} RPTQCL, respectively. The structures in Figs. 4(a) and 4(b) can be qualitatively analyzed with the three-level model of this section by using the following expression for the effective lifetime of the lower laser level 2, which is depopulated through RT into $2a$ and subsequently via electron-longitudinal-optical (e-LO) phonon scattering into the injector level(s) (i.e., the *resonant-phonon* scheme). The following expression can be derived using a two-level density matrix for levels 2 and $2a$ exclusively and assuming $2 \rightarrow 2a$ tunneling to be the only mechanism for carrier injection into level $2a$,²²

$$\tau_{2a,\text{eff}} = \tau_{2a} \left(\frac{2\Omega_{2,2a}^2 \tau_{\parallel} \tau_{2a} + \Delta_{2,2a}^2 \tau_{\parallel}^2 + 1}{2\Omega_{2,2a}^2 \tau_{\parallel} \tau_{2a}} \right). \quad (11)$$

The effective lower-level lifetime $\tau_{2a,\text{eff}}$, which is also

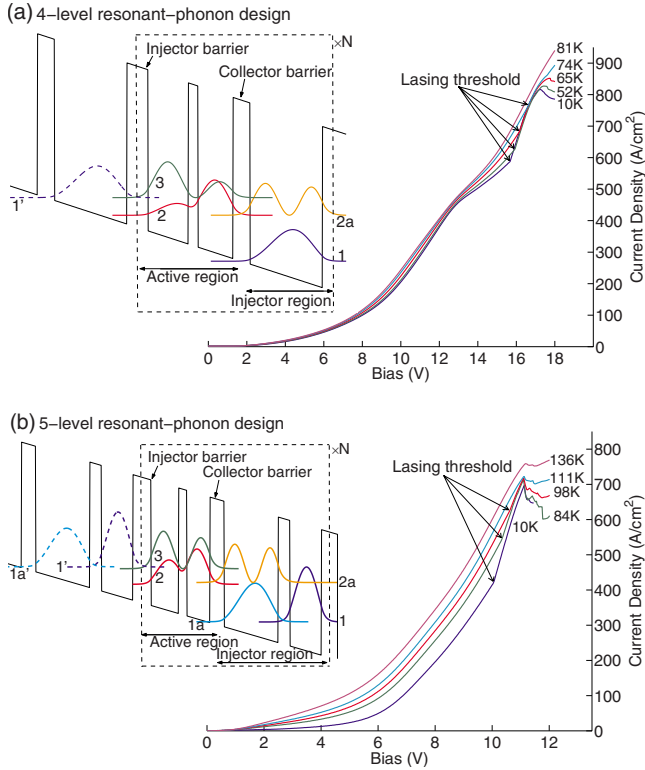


FIG. 4. (Color online) Typical experimental I - V 's versus temperature for (a) a four-level and (b) a five-level resonant-phonon terahertz QCL, respectively. The corresponding band diagrams show tight-binding wave functions at design bias calculated by splitting the QCL module into multiple submodules across the relevant barriers. The radiative transition is from $3 \rightarrow 2$, and the depopulation of the lower level is via $2 \rightarrow 2a$ RT and $2a \rightarrow 1/1a$ electron-longitudinal-optical phonon scattering where $E_{21} \approx \hbar\omega_{LO}$. The I - V 's are measured in cw operation for metal-metal ridge lasers. The plot in (a) is from a 3.9 THz QCL labeled OWI222G (Ref. 10) of dimensions $60 \mu\text{m} \times 310 \mu\text{m}$ ($T_{\text{max,cw}} \sim 76$ K) and that in (b) is from a 2.7 THz QCL labeled FL178C-M10 (Ref. 6) of dimensions $35 \mu\text{m} \times 670 \mu\text{m}$ ($T_{\text{max,cw}} \sim 108$ K). The onset of lasing results in a change in the slope of the I - V , which is indicated by arrows for the curves recorded below the $T_{\text{max,cw}}$.

equivalent to the *tunneling time* through the collector barrier, is plotted for three different values of the collector anticrossing $2\hbar\Omega_{2,2a}$ in Fig. 5. The best performing RPTQCLs have large collector anticrossings in the range of $2\hbar\Omega_{2,2a} \sim 4$ – 5 meV in which case $\tau_{2,\text{eff}}$ varies little in the operating bias range close to the 2 - $2a$ resonance ($\hbar\Delta_{2,2a} = 0$). For example, $2\hbar\Omega_{2,2a} \sim 4.7$ meV for the four-level QCL in Ref. 10 and the energy detuning $\hbar\Delta_{2,2a}$ approximately varies from -2 to 2.5 meV in operating bias range of the design. As seen from Fig. 5(a), $\tau_{2,\text{eff}}$ changes little within such a range of detuning.

We can similarly take the combined population $n_{\text{tot}} = n_1 + n_2 + n_3$ to be approximately bias independent. The population of level $2a$ is likely to be negligible due to its very short lifetime $\tau_{2a} \sim 0.2$ ps and that of level $1a$ in Fig. 4(b) is likely to vary negligibly with bias in the operating bias range of interest due to the typically large values of the intrainjector anticrossing $2\hbar\Omega_{1a,1} \sim 4$ – 5 meV in the five-

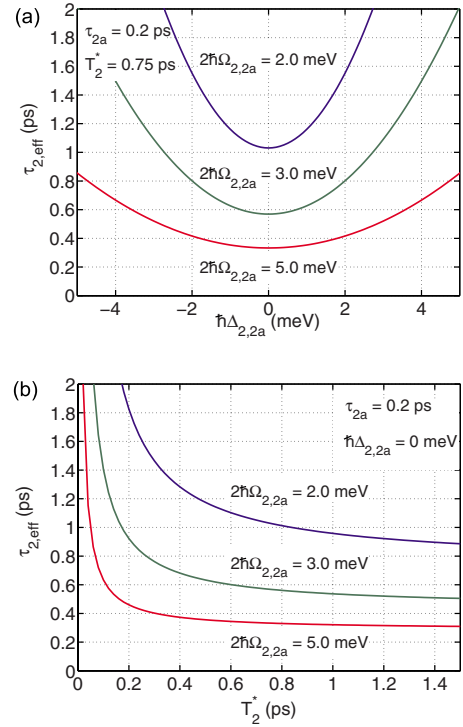


FIG. 5. (Color online) Plots of the effective lower-level lifetime $\tau_{2,\text{eff}}$ (also equivalent to the *tunneling time* through the collector barrier) for the resonant-phonon designs of the type shown in Fig. 4 calculated using Eq. (11). Plot (a) shows $\tau_{2,\text{eff}}$ versus the energy detuning $\hbar\Delta_{2,2a}$ between the levels 2 and $2a$ and (b) shows $\tau_{2,\text{eff}}$ versus the phenomenological dephasing time T_2^* calculated at the 2 - $2a$ resonance bias ($\hbar\Delta_{2,2a} = 0$). $\tau_{2a} \sim 0.2$ ps is assumed owing to the typical value obtained in GaAs/Al_{0.15}Ga_{0.85}As quantum wells for $E_{2a,1} \sim \hbar\omega_{LO}$.

level design Fig. 4(b). Given the bias independence of $n_{\text{tot}} = n_1 + n_2 + n_3$ and the lower-level lifetime $\tau_{2,\text{eff}}$ for the resonant-phonon designs in Fig. 4, we can now qualitatively compare the three-level model I - V 's in Fig. 3 to the experimental cw I - V 's in Fig. 4. For the latter, it can be noticed that J_{max} , which is characterized by the occurrence of a negative-differential-resistance region in the I - V , changes little up until the maximum operating temperature of the laser $T_{\text{max,cw}}$. However, beyond $T_{\text{max,cw}}$, the value of J_{max} increases with temperature. This characteristic is best described by the calculated I - V 's in Fig. 3(a) since the above-threshold current expression in Eq. (5) is independent of the upper-state to lower-state lifetime τ_{32} to a first order. Hence, it is likely that one of the dominant temperature degradation mechanism for RPTQCLs is a reduction in the upper-state (u) to lower-state (l) lifetime, which is mostly attributed to the thermally activated LO phonon scattering from the upper state.^{5,6} The recently developed terahertz QCL design with a very diagonal radiative transition is based on this observation to effectively increase the $u \rightarrow l$ lifetime at high temperatures.¹⁰ Additionally, it seems less likely that an increase in the effective lifetime of the lower state [potentially due to $1 \rightarrow 2$ thermal backfilling or increased dephasing for the $2 \rightarrow 2a$ RT that affects $\tau_{2,\text{eff}}$ as in Fig. 5(b)] or a broadening of the gain linewidth²⁸ are more dominant temperature degradation

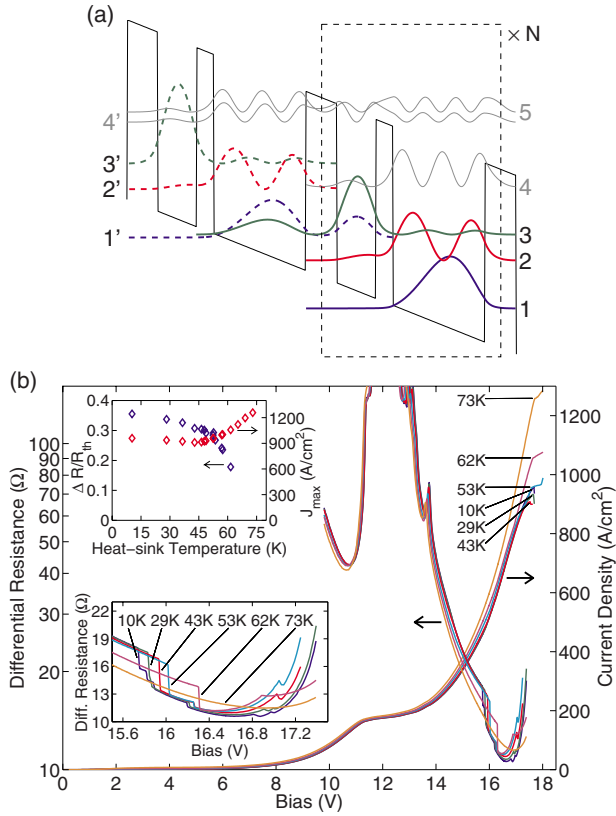


FIG. 6. (Color online) (a) Conduction-band diagram of a recently demonstrated two-well terahertz QCL design, labeled TW246 (Ref. 23). Only three levels (1, 2, and 3) participate in transport at low temperatures; however, at higher temperatures additional parasitic levels (4 and 5) are also likely to contribute to the current flow. (b) Experimental cw I - V 's and \mathcal{R} - V 's at different heat-sink temperatures from a $20 \mu\text{m} \times 1.56 \text{ mm}$ metal-metal ridge laser with a $T_{\text{max,cw}} \sim 63 \text{ K}$. The lasing threshold is marked by a discontinuity in the \mathcal{R} curves that is shown more clearly in an expanded view in the lower inset. The upper inset shows the variation in fractional discontinuity in \mathcal{R} at threshold $\frac{\Delta \mathcal{R}_{\text{th}}}{\mathcal{R}_{\text{th}}} (\equiv \frac{\mathcal{R}_{\text{th}} - \mathcal{R}_{\text{th}}^-}{\mathcal{R}_{\text{th}}})$ and of J_{max} with temperature.

mechanisms than that mentioned above; otherwise, the observed experimental behavior would have corresponded more closely with Fig. 3(e) or Fig. 3(c), respectively. That is, the peak current density J_{max} would decrease at elevated temperatures.

The two-well design of Fig. 1, which features an *intrawell-phonon* (IP) depopulation scheme as opposed to the RP depopulation scheme of Fig. 4, has also been experimentally realized recently.²³ The design-bias band diagram of the realized structure is shown in Fig. 6(a) including higher energy parasitic levels that are believed to contribute to electron transport at elevated temperatures. The experimental I - V 's and \mathcal{R} - V 's from a representative ridge laser in cw operation are shown in Fig. 6(b). The temperature variation in the I - V 's shows that J_{max} for this IP QCL decreases slightly with temperature up to $T \sim 45 \text{ K}$ and subsequently increases steeply with temperature until and beyond the $T_{\text{max,cw}} \sim 63 \text{ K}$. This unique dependence of J_{max} with T , also shown explicitly in the inset of Fig. 6(b), is different from

that of the RP QCLs in Fig. 4 and is attributed to the onset of a temperature degradation mechanism that is in addition to the reduction in τ_{32} due to thermally activated e-LO phonon scattering from $3 \rightarrow 2$. It is postulated that the lifetime of the upper state 3 decreases additionally due to absorption of nonequilibrium (hot) LO phonons via $3' \rightarrow (4', 5)$ scattering.²³ Any such scattered electrons quickly relax back eventually into the injector level of a neighboring module due to the short lifetime of the parasitic levels 4 and 5 ($\tau_{4'} \sim \tau_5 \sim 0.3 \text{ ps}$). Such a leakage mechanism can be considered approximately as an effective reduction in τ_{31} in order to apply the results of the three-level model to explain the behavior in Fig. 6(b), which then becomes consistent with calculated I - V behavior in Fig. 3(b). Note that the upper laser state in the RP designs is spatially isolated from the wide injector well(s) and hence from the higher energy parasitic levels.⁶ Hence, the aforementioned hot-phonon mediated leakage mechanism is weaker for the RPTQCLs as compared to the IP QCL structure of Fig. 6(a).

B. Discontinuity in differential resistance at threshold

The onset of lasing in a QCL is characterized by a slope discontinuity in its I - V characteristics.¹² This is a manifestation of the increased rate of carrier flow due to the stimulated emission process from the upper to the lower state, such that the population inversion is kept constant beyond threshold. The relative change in the differential resistance $\mathcal{R} = dV/dI$ of the device at threshold is a useful parameter since it is easily and accurately measurable and is shown below to be directly proportional to the value of Δn_{th} . We can relate the externally applied bias voltage across all the periods of the QCL to the energy detuning $\hbar \Delta_{1'3}$ as

$$V = \frac{\hbar \Delta_{1'3} N_p}{f_V |e|}, \quad (12)$$

where N_p is the number of repeated periods in the QCL structure and f_V is the fraction of per module voltage bias V/N_p that appears as the energy difference between levels 1' and 3. f_V is typically a slowly varying nonlinear function of the applied voltage V and is a characteristic of a particular design as shown in Fig. 7. For the main result presented in this section, the particular form of f_V is inconsequential and it is assumed to be a constant in the bias range right below and above the threshold. Using Eq. (12) the differential resistance \mathcal{R} becomes

$$\mathcal{R} = \frac{dV}{dI} \approx \frac{\hbar N_p}{f_V |e|} \frac{dE_{1'3}}{dI}. \quad (13)$$

In Eq. (13), we have dropped the term corresponding to $\frac{df_V}{dI}$ since f_V is approximately a constant as can be seen from Fig. 7. The calculations in Fig. 7 are done without accounting for band bending due to dopant-carrier segregation, which is typically insignificant due to the low doping in such QCL structures.¹⁹ The value of $\frac{df_V}{dI}$ is likely to be negligible in comparison to the leading term of Eq. (13) even if band bending were found to be significant for a particular design. We can now derive analytical expressions for the ratio as

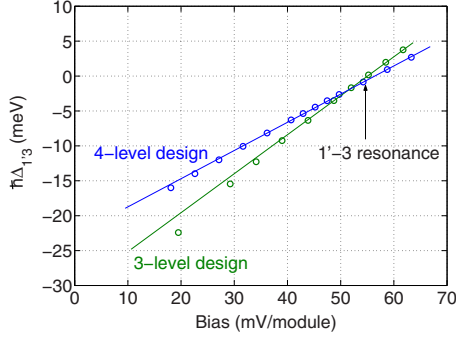


FIG. 7. (Color online) Detuning energy $\hbar\Delta_{1'3}$ as a function of the voltage per QCL module [$=V/N_p$ in Eq. (12)] for the tight-binding wave functions of the four-level resonant-phonon design of Fig. 4(a) and the three-level intrawell-phonon design of Fig. 6(a), respectively. Small circles represent calculated values, which are overlaid with straight line fits to the data points close to the 1'-3 resonance. The fits indicate that $\hbar\Delta_{1'3}$ is linearly related to V/N_p close to the 1'-3 resonance [i.e., f_V in Eq. (12) is a constant]. Typically, lasing threshold occurs after the 1'-2 resonance (~ 30 mV/module) beyond which the current continues to increase up to the 1'-3 resonance when J_{\max} occurs.

well as the fractional change in differential resistance just below ($\mathcal{R}_{\text{th}}^-$) and above ($\mathcal{R}_{\text{th}}^+$) threshold using Eq. (5) to calculate $\frac{d\Delta_{1'3}}{dI}$. The individual expressions for $\mathcal{R}_{\text{th}}^-$ and $\mathcal{R}_{\text{th}}^+$ are complicated; however, the ratio $\frac{\mathcal{R}_{\text{th}}^+}{\mathcal{R}_{\text{th}}^-}$ and hence the fractional change in \mathcal{R} at threshold $\frac{\Delta\mathcal{R}_{\text{th}}}{\mathcal{R}_{\text{th}}}$ is expressed in a surprisingly concise form as²²

$$\frac{\mathcal{R}_{\text{th}}^+}{\mathcal{R}_{\text{th}}^-} = \left[1 - \frac{2\Delta n_{\text{th}}}{n_{\text{tot}}} \left(\frac{1 - \frac{\tau_{21}}{2\tau_{31}}}{1 + \frac{\tau_{21}}{\tau_{31}}} \right) \right], \quad (14)$$

$$\frac{\Delta\mathcal{R}_{\text{th}}}{\mathcal{R}_{\text{th}}} \equiv \frac{\mathcal{R}_{\text{th}}^- - \mathcal{R}_{\text{th}}^+}{\mathcal{R}_{\text{th}}^-} = \frac{2\Delta n_{\text{th}}}{n_{\text{tot}}} \left(\frac{1 - \frac{\tau_{21}}{2\tau_{31}}}{1 + \frac{\tau_{21}}{\tau_{31}}} \right). \quad (15)$$

Note that Eq. (15) is derived for the case of unity injection efficiency, i.e., $\Omega_{1'2} \approx 0$ in the 3×3 DM Eq. (2). Hence, within the approximation that the current flow due to the $1' \rightarrow 2$ channel is negligible in comparison to the $1' \rightarrow 3$ channel at threshold, the expression derived for $\frac{\Delta\mathcal{R}_{\text{th}}}{\mathcal{R}_{\text{th}}}$ holds true irrespective of the nature of the RT transport (coherent or incoherent) across the injector barrier. At low temperatures, $\tau_{21} \ll \tau_{31}$ and hence $\frac{\Delta\mathcal{R}_{\text{th}}}{\mathcal{R}_{\text{th}}} \approx \frac{2\Delta n_{\text{th}}}{n_{\text{tot}}}$ gives an absolute measurement of the population inversion in the laser as a fraction of the combined populations of the injector level 1' and the laser levels 3 and 2 ($n_{\text{tot}} \equiv n_{1'} + n_2 + n_3$).

The slope efficiency of a QCL's optical power output is written as

$$\frac{dP_{\text{out}}}{dI} = \frac{N_p \hbar \omega_0}{|e|} \frac{\alpha_m}{(\alpha_w + \alpha_m)} \eta, \quad (16)$$

where ω_0 is the lasing frequency, α_m is the radiative (mirror) loss in the cavity, α_w is the material (waveguide) loss, and η is the internal quantum efficiency of the QCL structure. $\eta < 1$ due to the fact that n_3 and hence the nonradiative component of the current $I (=|e|n_3/\tau_3)$ continues to increase with I above threshold (even as $\Delta n = n_3 - n_2$ remains fixed at Δn_{th}), which causes the current above threshold ($I - I_{\text{th}}$) to be not entirely due to radiative transitions. An expression for η is derived as

$$\eta = \frac{1 - \frac{\tau_{21}}{\tau_{32}}}{1 + \frac{\tau_{21}}{\tau_{31}}} = 1 - \frac{\left. \frac{dn_3}{dI} \right|_{I=I_{\text{th}}^+}}{\left. \frac{dn_3}{dI} \right|_{I=I_{\text{th}}^-}}, \quad (17)$$

where

$$\left. \frac{dn_3}{dI} \right|_{I=I_{\text{th}}^+} = \frac{1}{|e|} \frac{\tau_{21}\tau_{31}}{(\tau_{21} + \tau_{31})},$$

$$\left. \frac{dn_3}{dI} \right|_{I=I_{\text{th}}^-} = \frac{1}{|e|} \tau_3. \quad (18)$$

Equation (17) for η can also be derived from a rate equation model since n_3 can be expressed in terms of I regardless of the nature of $1' \rightarrow 3$ RT transport. In literature,^{12,29} $\frac{\Delta\mathcal{R}_{\text{th}}}{\mathcal{R}_{\text{th}}}$ has similarly been derived from a rate equations approach, arguing that $n_3 \propto \Delta_{1'3}$, and hence the applied voltage V , in which case $\frac{\Delta\mathcal{R}_{\text{th}}}{\mathcal{R}_{\text{th}}}$ becomes same as η (for unity injection efficiency), and hence an indicator of the ratio of laser level lifetimes τ_{21}/τ_{32} . However, the expression for $\frac{\Delta\mathcal{R}_{\text{th}}}{\mathcal{R}_{\text{th}}}$ in Eq. (15) is starkly different from that of η in Eq. (17). While $\eta \rightarrow 1$ for $\tau_{21} \rightarrow 0$ but $\frac{\Delta\mathcal{R}_{\text{th}}}{\mathcal{R}_{\text{th}}} \rightarrow \frac{2\Delta n_{\text{th}}}{n_{\text{tot}}}$. Also, η strongly depends on the upper-state to lower-state lifetime τ_{32} , whereas $\frac{\Delta\mathcal{R}_{\text{th}}}{\mathcal{R}_{\text{th}}}$ is independent of τ_{32} . Hence, the result derived with the three-level DM model has important implications in the way the slope discontinuity is interpreted for the I - V of a QCL at threshold. In essence, $\frac{\Delta\mathcal{R}_{\text{th}}}{\mathcal{R}_{\text{th}}}$ is an indicator of the population inversion at threshold and not the ratio of level lifetimes, which are two different aspects of laser operation.

By means of Fig. 8, we now show that the assumption $n_3 \propto \Delta_{1'3}$, which is the basis of the previously held belief of $\frac{\Delta\mathcal{R}_{\text{th}}}{\mathcal{R}_{\text{th}}}$ being equivalent to η , is incorrect. For the conventional resonant-tunneling diode structures, carriers tunnel from the three-dimensional states in the emitter into the quasi-two-dimensional states in the well. Considering only first-order tunneling processes (i.e., conservation of in-plane momentum in tunneling through the barriers), the current flow is proportional to the Fermi energy μ_E in the emitter and hence the applied voltage V [as shown in Fig. 8(a), see Ref. 31, for example]. In such a case, the population n_1 of the subband 1 in Fig. 8(a) will indeed be proportional to V . However, for a semiconductor superlattice structure of which QCLs are specific examples, the current flow will be negligible if the sub-

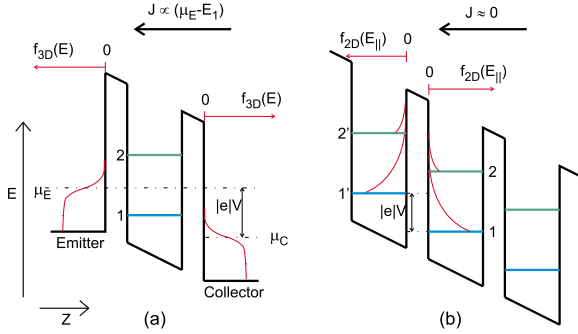


FIG. 8. (Color online) Illustrative band diagrams for (a) double-barrier resonant-tunneling diode structure (Ref. 30) that consists of a single quantum well sandwiched between degenerately doped emitter and collector regions, and (b) a superlattice structure (Ref. 1) that consists of multiple repeated quantum wells of which only three wells are shown. In (a), the shown Fermi distributions (indicated by thin red lines) for the carrier populations apply to a quasicontinuous carrier distribution in three dimensions, whereas in (b), the shown carrier distribution applies only to the two-dimensional momentum space in the x - y plane (since the carriers are confined in the z direction) and is typically Maxwell-Boltzmann type (i.e., the Fermi energy μ_n lies much below the energy of the bottom of the subband E_n indicated by thick horizontal lines). In (a), V is the voltage applied between the emitter and the collector that appears as the difference between the respective Fermi energies and in (b) V represents the voltage per repeated module of the superlattice that appears as the difference in the energy of the bottom of the subbands.

bands are significantly off-resonance in the neighboring quantum wells even if the carrier distributions overlap in energy. This is because total energy cannot be conserved in such a tunneling process since the in-plane momentum conservation needs to be satisfied. The applied bias field is in the z direction and hence affects the bottom energy of the subbands and their z -wave functions, however, the quasi-Fermi levels within the respective subbands represent the in-plane carrier distribution and are not directly affected by the applied voltage V . As a result, the subband populations cannot be assumed to be directly proportional to V . Instead, the subband populations and their thermal distributions (and hence the respective quasi-Fermi levels) are determined by the various intersubband and intrasubband scattering processes and also by the resonant-tunneling current flow induced by the coupling of the subband wave functions across the barriers as determined by the anticrossing energies $2\hbar\Omega_{ij}$ and detuning energies $\hbar\Delta_{ij}$. Note that higher order corrections to the resonant-tunneling current flow that relax the requirement of in-plane momentum conservation are not included in this simplified picture.^{18,32}

Figure 9 shows typical variation in $\frac{\Delta\mathcal{R}_{th}}{\mathcal{R}_{th}}$ with τ_{31} according to Eq. (15), which shows that $\frac{\Delta\mathcal{R}_{th}}{\mathcal{R}_{th}}$ decreases rapidly as τ_{31} becomes smaller and approaches τ_{21} . The trend in Fig. 9 could be compared to the experimental variation in $\frac{\Delta\mathcal{R}_{th}}{\mathcal{R}_{th}}$ with temperature for the two-well QCL shown in the upper inset of Fig. 6(b), which indicates a steady degradation of its effective τ_{31} with temperature due to a predicted hot-phonon effect.²³ Also note that J_{max} and $\frac{\Delta\mathcal{R}_{th}}{\mathcal{R}_{th}}$ in Fig. 6(b) have a

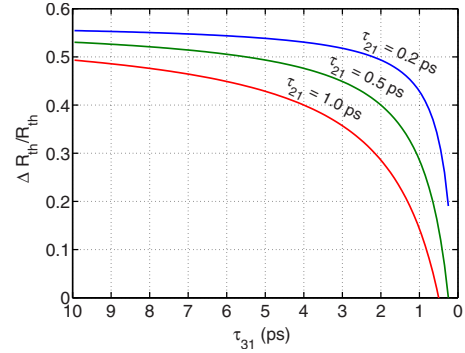


FIG. 9. (Color online) Variation in the fractional change in differential resistance at threshold $\frac{\Delta\mathcal{R}_{th}}{\mathcal{R}_{th}}$ with τ_{31} calculated using the expression in Eq. (15) with same typical values of different parameters as in Fig. 3.

correlated behavior where $J_{max} \uparrow$ as $\frac{\Delta\mathcal{R}_{th}}{\mathcal{R}_{th}} \downarrow$. This validates the expression in Eq. (5) for operation above threshold, which suggests $J_{max} \propto (1 - \frac{\Delta\mathcal{R}_{th}}{\mathcal{R}_{th}})$, where J_{max} is the current flowing at 1'-3 resonance ($\Delta_{1'3}=0$) and Eq. (15) is used for substitution. For this IP QCL also, gain bandwidth broadening with temperature is less likely to be the dominant temperature degradation mechanism. Otherwise, the value of $\frac{\Delta\mathcal{R}_{th}}{\mathcal{R}_{th}}$ should increase according to Eq. (15) with the requirement of a larger population inversion to reach threshold.

III. OPTICAL GAIN SPECTRUM OF RESONANT-PHONON TERAHERTZ QCLS

Terahertz QCL designs with RP depopulation typically have broad gain linewidths. The spontaneous emission spectra from one of the earliest such designs had a ~ 2 THz full-width half-maximum (FWHM) linewidth for a ~ 4 THz QCL active region.¹⁹ Experimental spontaneous emission data for some of the more recent high performance designs^{10,33} is not available because of the difficulty in observing subthreshold optical signal in metal-metal waveguides,³⁴ both because of the low loss in these waveguides that causes lasing soon after the upper level is populated with electrons and also due to the poor out-coupling efficiency of such cavities.³⁵ However, simultaneous lasing of modes separated by frequencies greater than 0.5 THz (Refs. 20 and 36) suggests that large gain exists over a broad bandwidth that is a significant fraction of the center frequency in a homogeneously grown RPTQCL design (in contrast to heterogeneous cascade designs that have been used to realize broad gain bandwidths at mid-infrared frequencies³⁷).

In this section, we use density matrices to numerically estimate the optical gain spectrum in a RPTQCL design and find reasons for broadening of the gain spectrum. Similar to the I - V calculations in Sec. II, the simplified DM calculations are shown to be an effective method to understand the role of various design parameters toward the optical response of a terahertz QCL gain medium, as opposed to the nonequilibrium Green's function technique that incorporates a full

quantum theory of gain.^{38,39} Similar calculations have been used recently to determine the optimal injector coupling in mid-infrared QCLs (Ref. 40) and also to describe the electrical transport characteristics of RT extraction based terahertz QCL structure.¹⁴ We consider the simplest RP design with four levels per QCL period as shown in Fig. 10. To compute the gain (or loss) spectrum, the linear response to a

sinusoidal electric field perturbation of the form $\mathbf{E} = \hat{z}\mathcal{E}(e^{+i\omega t} + e^{-i\omega t})$ is calculated by incorporating the electric dipole interaction term for coherent coupling of the radiative levels. Only the electric field component in the growth direction \hat{z} is considered due to the intersubband polarization selection rule. The time evolution of the DM for the four-level design is then written as²²

$$\frac{d}{dt} \begin{pmatrix} \rho_{1'1'} & \rho_{1'4} & \rho_{1'3}e^{+i\omega t} & \rho_{1'2}e^{+i\omega t} \\ \rho_{41'} & \rho_{44} & \rho_{43}e^{+i\omega t} & \rho_{42}e^{+i\omega t} \\ \rho_{31'}e^{-i\omega t} & \rho_{34}e^{-i\omega t} & \rho_{33} & \rho_{32} \\ \rho_{21'}e^{-i\omega t} & \rho_{24}e^{-i\omega t} & \rho_{23} & \rho_{22} \end{pmatrix} = -\frac{i}{\hbar} \begin{pmatrix} E_{1'} & -\hbar\Omega_{1'4} & 0 & 0 \\ -\hbar\Omega_{1'4} & E_4 & |e|z_{43}\mathcal{E}e^{+i\omega t} & 0 \\ 0 & |e|z_{43}\mathcal{E}e^{-i\omega t} & E_3 & -\hbar\Omega_{32} \\ 0 & 0 & -\hbar\Omega_{32} & E_2 \end{pmatrix} \bar{\rho}_{(1',4,3,2)} + \begin{pmatrix} \frac{\rho_{44} + \rho_{22}}{\tau_{41} + \tau_{21}} & -\frac{\rho_{1'4}}{\tau_{\parallel 14}} & -\frac{\rho_{1'3}e^{+i\omega t}}{\tau_{\parallel 13}} & -\frac{\rho_{1'2}e^{+i\omega t}}{\tau_{\parallel 12}} \\ -\frac{\rho_{41'}}{\tau_{\parallel 14}} & -\frac{\rho_{44} - \rho_{44} - \rho_{33}}{\tau_4 + \tau_{st}} & -\frac{\rho_{43}e^{+i\omega t}}{\tau_{\parallel 34}} & -\frac{\rho_{42}e^{+i\omega t}}{\tau_{\parallel 24}} \\ -\frac{\rho_{31'}e^{-i\omega t}}{\tau_{\parallel 13}} & -\frac{\rho_{34}e^{-i\omega t}}{\tau_{\parallel 34}} & \frac{\rho_{44} + \rho_{44} - \rho_{33}}{\tau_{43} + \tau_{st}} & -\frac{\rho_{32}}{\tau_{\parallel 23}} \\ -\frac{\rho_{21'}e^{-i\omega t}}{\tau_{\parallel 12}} & -\frac{\rho_{24}e^{-i\omega t}}{\tau_{\parallel 24}} & -\frac{\rho_{23}}{\tau_{\parallel 23}} & -\frac{\rho_{22}}{\tau_{21}} \end{pmatrix}. \quad (19)$$

Equation (19) is written similarly as Eq. (2) with additional modifications due to the sinusoidal electric field perturbation. We consider linear response within the rotating-wave approximation (i.e., $|\omega - \omega_{43}| \ll \omega$) in which case the affected coherences can be explicitly written to have a sinusoidal time variation as shown with the slowly varying amplitudes ρ_{mn} . The radiative levels 3 and 4 are now coherently coupled through the off-diagonal electric dipole interaction term $|e|\mathbf{r}\cdot\mathbf{E}$ that has an amplitude $|e|z_{43}\mathcal{E}$, where $z_{43} = \langle 4|\hat{z}|3\rangle$ is the dipole-matrix element for the said tight-binding levels. Since $(1', 4)$ and $(3, 2)$ are coherently coupled due to nonzero $\Omega_{1'4}$ and Ω_{32} terms, respectively, the coherences corresponding to $(1', 3)$, $(1', 2)$, and $(4, 2)$ acquire a time-harmonic character due to the time-harmonic $(4, 3)$ coherent coupling. The sinusoidal component of the coherences is written explicitly in the ansatz $\rho_{(1',4,3,2)}$ in which case $\frac{d\rho_{mn}}{dt} = 0$ in the steady state for the slowly varying amplitudes ρ_{mn} . Note that $\bar{\rho}_{(1',4,3,2)}$ on the right side of Eq. (19) is the same as the left-side matrix appearing with the time derivative.

We made some simplifying approximations in writing Eq. (19). Similar to before, for simplicity of calculations, we assume a unity injection efficiency ($\Omega_{1'3} \approx 0$), also a unity collection efficiency ($\Omega_{42} \approx 0$), and neglect the backscattering terms τ_{12} and τ_{34} . For nonzero $\Omega_{1'3}$ and/or Ω_{42} , Eq. (19) will become more complicated since some of the nonharmonic terms in the $\bar{\rho}_{(1',4,3,2)}$ matrix will additionally acquire time-harmonic character and similarly some of the time-

harmonic coherences will additionally acquire a constant value in the steady state, thereby effectively increasing the number of independent variables to be solved for the system (currently 16 for the written equation). Also, a parameter τ_{41}

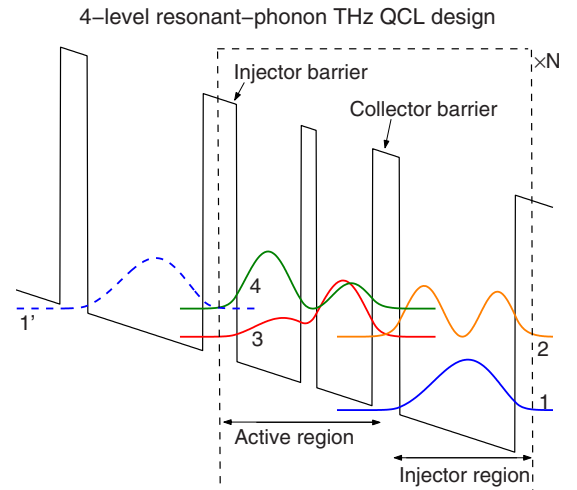


FIG. 10. (Color online) The four-level resonant-phonon terahertz QCL structure reproduced from Fig. 4(a) with a different level numbering scheme for simplicity of presentation in the following discussions. The radiative transition is from $4 \rightarrow 3$, and depopulation of the lower level is via $3 \rightarrow 2$ RT and $2 \rightarrow 1$ e-LO phonon scattering where $E_{21} \approx \hbar\omega_{LO}$.

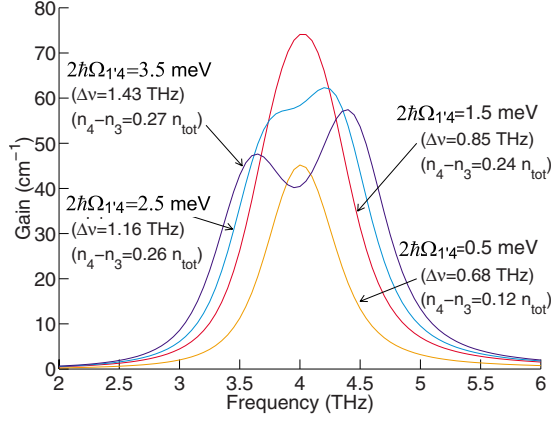


FIG. 11. (Color online) Computed gain spectra for the four-level structure of Fig. 10 for different injector anticrossings $2\hbar\Omega_{1'4}$, evaluated at $1'-4$ resonance ($\Delta_{1'4}=0$). Levels 3 and 2 are also taken to be at resonance ($\Delta_{32}=0$) and a small value of $2\hbar\Omega_{32}=2$ meV is chosen to limit additional broadening due to a coherent $3\rightarrow 2$ RT process [as shown in Fig. 12(a)]. All other parameters have same equivalent values as in Fig. 3, except $\tau_{21}=0.2$ ps that results in an effective lower-state lifetime $\tau_{3,\text{eff}}(\equiv \frac{n_3}{n_2}\tau_{21})\approx 1.0$ ps, which can also be estimated from the equivalent of Eq. (11). Also, $E_{43}=16.5$ meV (4 THz). The values of FWHM linewidth $\Delta\nu$ and population inversion $\Delta n_{43}=n_4-n_3$ obtained as a result of the calculation are also indicated alongside each of the curves.

is included to incorporate the effect of any indirect parasitic scattering channels from 4 to 1 since direct $4\rightarrow 1$ transport is otherwise only allowed via intersubmodule tunneling across the collector barrier for the chosen set of tight-binding basis functions. We can now solve this equation, which, in addition to yielding values of current and level populations, also yields the electrical polarization $\hat{\mathcal{P}}(t)$ induced due to the external optical field \mathbf{E} as

$$\begin{aligned}\mathcal{P} &\equiv \epsilon_0\chi(\omega)\mathcal{E}e^{+i\omega t} + \text{c.c.} \\ &= \frac{-|e|\langle\hat{z}\rangle}{V_{\text{ac}}} \\ &= \frac{-|e|z_{43}}{V_{\text{ac}}}\{[\rho_{43}(\omega) + \rho_{34}(-\omega)]e^{+i\omega t} + \text{c.c.}\},\end{aligned}\quad (20)$$

where V_{ac} is the volume of the active region. The induced electrical susceptibility $\chi(\omega)$ becomes

$$\chi(\omega) \equiv \chi'(\omega) + i\chi''(\omega) = \frac{-|e|z_{43}}{V_{\text{ac}}\epsilon_0\mathcal{E}}[\rho_{43}(\omega) + \rho_{34}(-\omega)],\quad (21)$$

which is independent of the amplitude \mathcal{E} for small values. The optical gain coefficient $g(\omega)$ (per meter) is related to the imaginary part of the susceptibility $\chi''(\omega)$ as

$$g(\omega)|_{(\chi',\chi'')\ll n_r^2} = \frac{\chi''(\omega)}{n_r} \frac{\omega}{c},\quad (22)$$

where n_r is the refractive index of the medium. In the following, we show results of the computed gain spectrum as a function of several different parameters of interest.

A. Optical gain spectrum as a function of injector anticrossing

Figure 11 shows the numerically computed gain spectra for the four-level RPTQCL design as modeled by Eq. (19) for different values of injector anticrossing $2\hbar\Omega_{1'4}$. For the $4\rightarrow 3$ radiative transition, the FWHM frequency linewidth due to scattering is given by $\Delta\nu_{\text{scatt}}\approx\frac{1}{\pi}\left[\frac{1}{2\tau_{3,\text{eff}}}+\frac{1}{2\tau_4}+\frac{1}{T_2^*}\right]$, which yields a value of 0.67 THz ($h\Delta\nu_{\text{scatt}}\sim 2.75$ meV) for the chosen parameters. The value of $T_2^*=0.75$ ps was assumed for the above value of the linewidth to approximately agree with those observed typically for bound-to-continuum THz QCLs (Refs. 41–43) whose linewidths are more likely to be scattering limited. As $2\hbar\Omega_{1'4}$ becomes as large as $h\Delta\nu_{\text{scatt}}$, injector transport becomes more coherent and the gain spectrum becomes additionally broadened due to anti-crossing splitting of the linewidth as can be seen from Fig. 11. Also note that the population inversion Δn approaches the maximum value given by Eq. (7) for coherent injection, which, for the present case yields $\Delta n_{\text{max}}\sim\left(\frac{1-\tau_{3,\text{eff}}/\tau_{43}}{2+\tau_{3,\text{eff}}/\tau_{43}}\right)n_{\text{tot}}\approx 0.28n_{\text{tot}}$. The area under the gain curve is proportional to the population inversion Δn_{43} , therefore, any additional broadening decreases the peak gain. This suggests that a value of $2\hbar\Omega_{1'4}$ much larger than $h\Delta\nu_{\text{scatt}}$ might in fact diminish the performance of a design. However, as will be shown in the next section, RPTQCL designs anyway have broad linewidths due to a coherent RT assisted depopulation process in which case having $2\hbar\Omega_{1'4}>h\Delta\nu_{\text{scatt}}$ is less likely to cause additional broadening of the gain linewidth. Consequently, the injector anticrossing value for the RPTQCL designs is chosen based on other design parameters such as the $1'\rightarrow 3$ parasitic current leakage¹⁰ rather than the concerns about gain broadening.

B. Optical gain spectrum as a function of collector anticrossing

Figures 12(a) and 12(b) show the computed gain spectra for different values of collector anticrossings $2\hbar\Omega_{32}$ and energy detuning $\hbar\Delta_{32}$, respectively. The best RPTQCL designs typically have collector anticrossing values in the range of 4–5 meV. This is to maintain a short effective lower-state lifetime so as to maximize $J_{\text{max}}/J_{\text{th}}$ since $J_{\text{max}}\propto\tau_{\text{lower}}^{-1}$ for coherent injection [Eq. (8)], although at the cost of a broader linewidth. For example, the $2\hbar\Omega_{32}=5$ meV spectrum in Fig. 12(a) has a FWHM linewidth of 1.8 THz, a value almost twice as large as the scattering linewidth $\Delta\nu_{\text{scatt}}\sim 1$ THz (calculated using $\tau_{3,\text{eff}}\sim 0.3$ ps). This shows that the anti-crossing splitting of the gain spectrum due to the coherent RT assisted depopulation process is the main cause of the broad linewidths associated with RPTQCLs.^{19,20,36} As seen from Fig. 12(b), note that linewidth broadening happens only close to the 3-2 resonance at $\hbar\Delta_{32}\approx 0$. For $|\hbar\Delta_{32}|>0$ and $|\hbar\Delta_{32}|\ll E_{43}$, the width of the spectrum remains narrow since the $4\rightarrow 2$ radiative transition (which is indirect, and due to $4\leftrightarrow 3$ and $3\leftrightarrow 2$ coherent coupling) is considerably detuned from the stronger $4\rightarrow 3$ radiative transition (which is direct and due to $4\leftrightarrow 3$ coherent coupling), and hence contributes negligibly to the gain. For a coherent $3\rightarrow 2$ RT process (i.e., large Ω_{32}), the peak gain occurs at a frequency

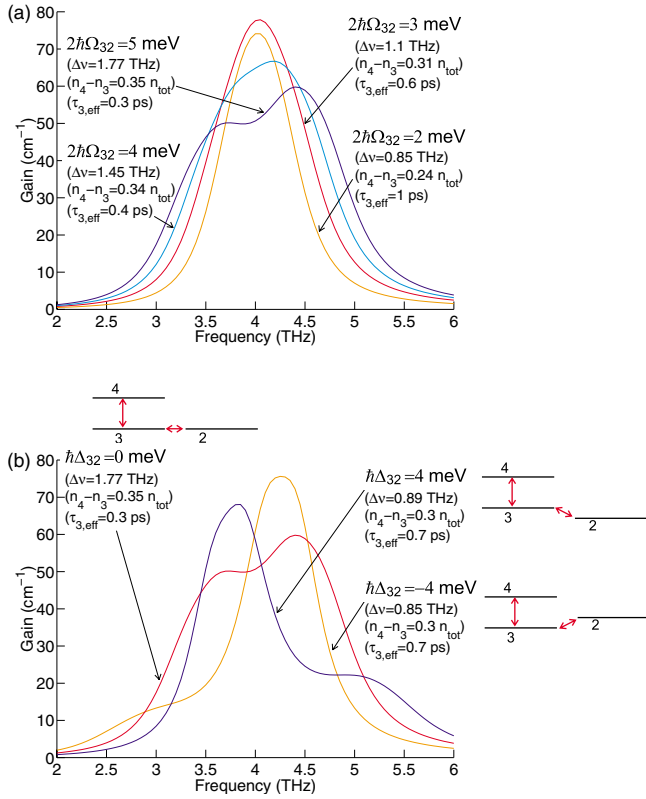


FIG. 12. (Color online) Computed gain spectra for the four-level QCL design of Fig. 10 for (a) different values of collector anticrossings $2\hbar\Omega_{32}$ at resonance ($\Delta_{32}=0$) and (b) different values of detuning $\hbar\Delta_{32}$ at $2\hbar\Omega_{32}=5$ meV. Levels $1'$ and 4 are assumed to be at resonance ($\Delta_{1'4}=0$) and a small value of $2\hbar\Omega_{1'4}=1.5$ meV is chosen to limit additional broadening due to a coherent $1' \rightarrow 4$ RT process (as shown in Fig. 11). Other parameters are the same as in Fig. 11. The values of FWHM linewidth $\Delta\nu$, effective lifetime of the lower state $\tau_{3,\text{eff}} (\equiv \frac{n_3}{n_2} \tau_{21})$, and population inversion $\Delta n_{43}=n_4-n_3$ obtained as a result of the calculation are also indicated alongside each of the curves.

$\omega_{\text{peak}} > E_{43}/\hbar$ for $\hbar\Delta_{32} < 0$ and $\omega_{\text{peak}} < E_{43}/\hbar$ for $\hbar\Delta_{32} > 0$. The frequency shift of ω_{peak} away from E_{43}/\hbar is due to the energy splitting due to the 3-2 anticrossing close to resonance.

We now show computed gain spectra of the four-level RPTQCL design from Ref. 10 in Fig. 13(a) as a function of applied electrical bias. For a comparison, experimentally measured cw I - V and lasing spectra of a ridge laser processed from the same active medium is also shown in Fig. 13(b). For the calculation in Fig. 13(a), the radiative energy E_{43} varies linearly from 12.4 meV (3.0 THz) at 8 V to 15.7 meV (3.8 THz) at the $1'$ - 4 resonance bias of 12 V due to the large value of the Stark shift in a diagonal radiative transition. However, the peak gain occurs close to a frequency of 4 THz at almost all bias conditions for the calculated spectra. This behavior is due to the coherent nature of the depopulation process. The 3-2 energy detuning $\hbar\Delta_{32}$ also varies linearly with the applied bias, from -4.7 meV at 8 V to 2.4 meV at 12 V. Consequently, as shown by the calculations in Fig. 12(b), the gain peak is pushed to higher frequencies than the radiative separation E_{43} at low bias that effectively masks

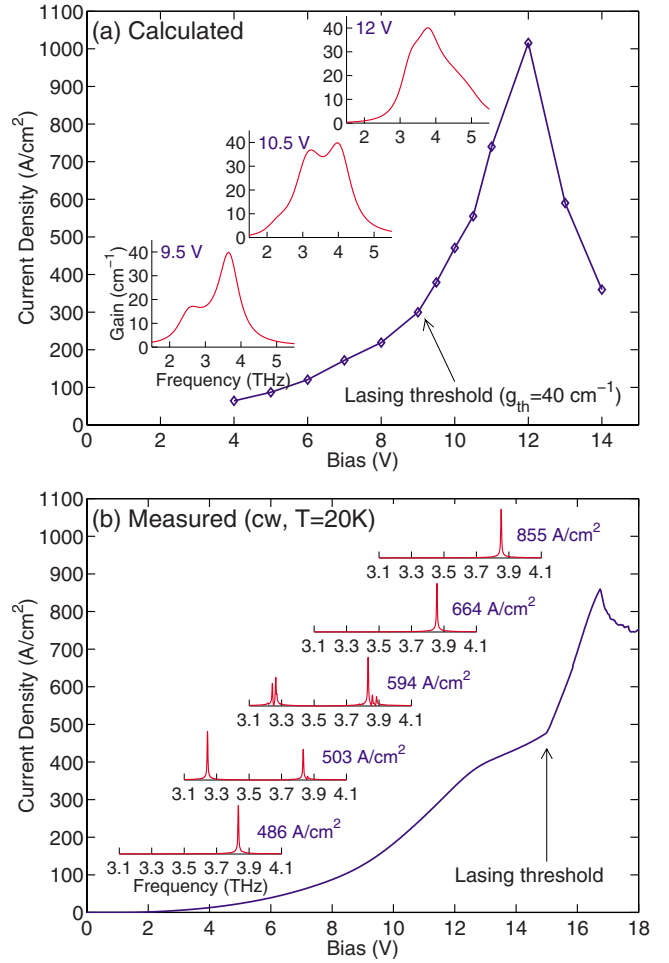


FIG. 13. (Color online) (a) Computed I - V and gain spectra at selected bias points for the four-level QCL in Ref. 10. These results are obtained by solving Eq. (19) in the steady state ($\frac{d}{dt} \rightarrow 0$), whereby, $I \equiv |e| (\frac{p_{44}}{\tau_{41}} + \frac{p_{22}}{\tau_{21}})$ and the gain is calculated using Eq. (22). A value of $g_{\text{th}}=40$ cm⁻¹ is assumed similar to that for Fig. 3 (Ref. 25) following which the stimulated lifetime τ_{st} is determined to keep the peak gain constant as g_{th} beyond threshold. Nonradiative lifetimes are calculated by including e-LO phonon scattering only whereby an electron temperature of 100 K is assumed in the upper level 4. Also, $T_2^* \sim 0.75$ ps and $\Omega_{1'3} \approx \Omega_{42} \approx 0$. (b) Experimental I - V and spectra (shown as insets) at selected bias points measured at a heat-sink temperature of 20 K in cw mode. The device is a $100 \mu\text{m} \times 1.39$ mm metal-metal waveguide ridge laser from the same active region as in Ref. 10. The higher than expected bias voltages for the experimental I - V are likely due to additional voltage drop at the electrical contacts.

the Stark shift in E_{43} . This is affirmed from the lasing spectra in Fig. 13(b) that shows that the ~ 3.9 THz mode is excited at all bias. In contrast, the Stark shift is clearly emphasized in the lasing mode spectrum of the diagonal bound-to-continuum terahertz QCLs (Ref. 7) due to the different depopulation mechanism in such designs.

As an evidence of the broad gain linewidth in this QCL, at some middle-bias points, additional lasing spectra are excited close to a frequency of 3.3 THz that leads to simultaneous cw lasing of modes separated by ~ 0.6 THz. This behavior could be attributed to the double-peaked gain spectra

that emerges close to the 3-2 resonance ($\Delta_{32} \approx 0$), which, for this design, happens at the middle-bias points. It may be noted that we have observed similar dual-frequency lasing behavior in some versions of the five-level RPTQCL design of Fig. 4(b). Whether or not this happens depends on the relative alignment of the injector and collector anticrossings as a function of the applied electrical bias.

We should note that recently a much smaller FWHM linewidth of ~ 0.6 THz has been measured for a similar four-level RPTQCL design⁴⁴ using a THz time-domain spectroscopy technique, which could be due to the following reasons. The QCL structure in Ref. 44 has a smaller collector anticrossing $2\hbar\Omega_{32} \sim 3.7$ meV as opposed to a value of $2\hbar\Omega_{32} \sim 4.7$ meV for the design in Ref. 10 that is analyzed in Fig. 13. Also, it is possible for a given QCL structure that the bias range of lasing operation may not sweep through its collector resonance ($\Delta_{32}=0$) depending on the relative alignment of the injector and the collector anticrossings for the grown structure in which case the gain spectra may not show additional broadening due to the $3 \rightarrow 2$ RT as seen from some specific calculations for nonzero $\hbar\Delta_{32}$ in Fig. 12(b). We would also like to note that the present calculations were done within a rotating-wave approximation ($|\omega - \omega_{43}| \ll \omega$), which becomes less accurate once the gain linewidth becomes a significant fraction of the center frequency. Hence, the true linewidths may be somewhat narrower than those calculated in this section. Nevertheless, within the assumptions considered, the close tracking of the calculated and experimental spectral characteristics of the four-level RPTQCL design in Fig. 13 establishes the importance of the

relatively simple density-matrix model developed in this section for estimating the optical gain spectrum of a terahertz QCL structure.

In conclusion, we have presented simplified density-matrix transport models to describe resonant-tunneling transport in terahertz QCLs. Due to the closely spaced energy levels in terahertz QCL structures, coherence plays an important role in the resonant-tunneling mechanism, which is incorporated well within the presented framework. A three-level model was developed to derive current transport through the injector barrier of any general QCL design (which applies to mid-infrared QCLs as well). Useful expressions were derived for current flow above and below threshold that could directly be used to analyze the experimental behavior of some representative QCL designs. Based on experimental observations, we have been able to speculate about some of the dominant temperature degradation mechanisms in phonon-depopulated terahertz QCL designs. We have extended the density-matrix model to estimate the gain spectra of resonant-phonon terahertz QCLs. A coherent resonant-tunneling assisted depopulation process is identified to be the primary cause of the broad gain bandwidths typically observed in such QCLs.

ACKNOWLEDGMENTS

We would like to thank Chun W. I. Chan for assistance with some of the experimental work reported here. This work is supported by AFOSR, NASA, and NSF.

¹L. Esaki and R. Tsu, IBM J. Res. Dev. **14**, 61 (1970).

²R. F. Kazarinov and R. A. Suris, Sov. Phys. Semicond. **5**, 707 (1971).

³J. Faist, F. Capasso, D. L. Sivco, C. Sirtori, A. L. Hutchinson, and A. Y. Cho, Science **264**, 553 (1994).

⁴R. Köhler, A. Tredicucci, F. Beltram, H. E. Beere, E. H. Linfield, A. G. Davies, D. A. Ritchie, R. C. Iotti, and F. Rossi, Nature (London) **417**, 156 (2002).

⁵B. S. Williams, Nat. Photonics **1**, 517 (2007).

⁶S. Kumar and A. W. M. Lee, IEEE J. Sel. Top. Quantum Electron. **14**, 333 (2008).

⁷G. Scalari, C. Walther, M. Fischer, R. Terazzi, H. Beere, D. Ritchie, and J. Faist, Laser Photonics Rev. **3**, 45 (2009).

⁸B. S. Williams, H. Callebaut, S. Kumar, Q. Hu, and J. L. Reno, Appl. Phys. Lett. **82**, 1015 (2003).

⁹Q. Hu, B. S. Williams, S. Kumar, H. Callebaut, S. Kohen, and J. L. Reno, Semicond. Sci. Technol. **20**, S228 (2005).

¹⁰S. Kumar, Q. Hu, and J. L. Reno, Appl. Phys. Lett. **94**, 131105 (2009).

¹¹A. Wade, G. Fedorov, D. Smirnov, S. Kumar, B. S. Williams, Q. Hu, and J. L. Reno, Nat. Photonics **3**, 41 (2009).

¹²C. Sirtori, F. Capasso, J. Faist, A. L. Hutchinson, D. L. Sivco, and A. Y. Cho, IEEE J. Quantum Electron. **34**, 1722 (1998).

¹³R. Terazzi, T. Gresch, A. Wittmann, and J. Faist, Phys. Rev. B **78**, 155328 (2008).

¹⁴G. Scalari, R. Terazzi, M. Giovannini, N. Hoyler, and J. Faist, Appl. Phys. Lett. **91**, 032103 (2007).

¹⁵G. Scalari, M. I. Amanti, M. Fischer, R. Terazzi, C. Walther, M. Beck, and J. Faist, Appl. Phys. Lett. **94**, 041114 (2009).

¹⁶H. Callebaut and Q. Hu, J. Appl. Phys. **98**, 104505 (2005).

¹⁷R. F. Kazarinov and R. A. Suris, Sov. Phys. Semicond. **6**, 120 (1972).

¹⁸H. Willenberg, G. H. Döhler, and J. Faist, Phys. Rev. B **67**, 085315 (2003).

¹⁹B. S. Williams, Ph.D. dissertation, Massachusetts Institute of Technology, 2003.

²⁰S. Kumar, B. S. Williams, Q. Qin, A. W. M. Lee, Q. Hu, and J. L. Reno, Opt. Express **15**, 113 (2007).

²¹S.-C. Lee, F. Banit, M. Woerner, and A. Wacker, Phys. Rev. B **73**, 245320 (2006).

²²S. Kumar, Ph.D. dissertation, Massachusetts Institute of Technology, 2007.

²³S. Kumar, C. W. I. Chan, Q. Hu, and J. L. Reno, Appl. Phys. Lett. **95**, 141110 (2009).

²⁴F. Eickemeyer, K. Reimann, M. Woerner, T. Elsaesser, S. Barbieri, C. Sirtori, G. Strasser, T. Müller, R. Bratschitsch, and K. Unterrainer, Phys. Rev. Lett. **89**, 047402 (2002).

²⁵The value of 40 cm^{-1} for the threshold material gain g_{th} was chosen based on some published estimates. For single-plasmon waveguides (Ref. 4), values of $\sim 25 \text{ cm}^{-1}$ have been estimated

- experimentally for the modal gain threshold of 1 mm long cavities with a 3.1 THz (Ref. 44) and a 4.3 THz (Ref. 45) resonant-phonon QCL gain medium, respectively. This results in $g_{\text{th}} > 70 \text{ cm}^{-1}$ for such waveguides given their low mode-confinement factors [25–35 % (Ref. 35)]. In contrast, metal-metal waveguides (Ref. 34) have lower losses (Ref. 35), with the lone published experimental estimate being $g_{\text{th}} \sim 36 \pm 10 \text{ cm}^{-1}$ for a 3.6 THz bound-to-continuum QCL (Ref. 46).
- ²⁶H. Luo, S. R. Laframboise, Z. R. Wasilewski, G. C. Aers, H. C. Liu, and J. C. Cao, *Appl. Phys. Lett.* **90**, 041112 (2007).
- ²⁷S. Kumar, B. S. Williams, Q. Hu, and J. L. Reno, *Appl. Phys. Lett.* **88**, 121123 (2006).
- ²⁸R. Nelander and A. Wacker, *Appl. Phys. Lett.* **92**, 081102 (2008).
- ²⁹L. Ajili, G. Scalari, J. Faist, H. Beere, E. Linfield, D. Ritchie, and G. Davies, *Appl. Phys. Lett.* **85**, 3986 (2004).
- ³⁰L. L. Chang, L. Esaki, and R. Tsu, *Appl. Phys. Lett.* **24**, 593 (1974).
- ³¹H. Ohno, E. E. Mendez, and W. I. Wang, *Appl. Phys. Lett.* **56**, 1793 (1990).
- ³²A. Wacker, *Adv. Solid State Phys.* **41**, 199 (2001).
- ³³B. S. Williams, S. Kumar, Q. Hu, and J. L. Reno, *Opt. Express* **13**, 3331 (2005).
- ³⁴B. S. Williams, S. Kumar, H. Callebaut, Q. Hu, and J. L. Reno, *Appl. Phys. Lett.* **83**, 2124 (2003).
- ³⁵S. Kohen, B. S. Williams, and Q. Hu, *J. Appl. Phys.* **97**, 053106 (2005).
- ³⁶B. S. Williams, S. Kumar, Q. Hu, and J. L. Reno, *Opt. Lett.* **30**, 2909 (2005).
- ³⁷R. Maulini, A. Mohan, M. Giovannini, J. Faist, and E. Gini, *Appl. Phys. Lett.* **88**, 201113 (2006).
- ³⁸S.-C. Lee and A. Wacker, *Phys. Rev. B* **66**, 245314 (2002).
- ³⁹A. Wacker, R. Nelander, and C. Weber, *Proc. SPIE* **7230**, 72301A (2009).
- ⁴⁰J. B. Khurgin, Y. Dikmelik, P. Q. Liu, A. J. Hoffman, M. D. Escarra, K. J. Franz, and C. F. Gmachl, *Appl. Phys. Lett.* **94**, 091101 (2009).
- ⁴¹G. Scalari, L. Ajili, J. Faist, H. Beere, E. Linfield, D. Ritchie, and G. Davies, *Appl. Phys. Lett.* **82**, 3165 (2003).
- ⁴²J. Kröll, J. Darmo, S. S. Dhillon, X. Marcadet, M. Calligaro, C. Sirtori, and K. Unterrainer, *Nature (London)* **449**, 698 (2007).
- ⁴³N. Jukam, S. S. Dhillon, D. Oustinov, Z.-Y. Zhao, S. Hameau, J. Tignon, S. Barbieri, A. Vasanelli, P. Filloux, C. Sirtori, and X. Marcadet, *Appl. Phys. Lett.* **93**, 101115 (2008).
- ⁴⁴N. Jukam, S. S. Dhillon, D. Oustinov, J. Madéo, J. Tignon, R. Colombelli, P. Dean, M. Salih, S. P. Khanna, E. H. Linfield, and A. G. Davies, *Appl. Phys. Lett.* **94**, 251108 (2009).
- ⁴⁵S. Kumar, A. W. M. Lee, Q. Qin, B. S. Williams, Q. Hu, and J. L. Reno, *Proc. SPIE* **6909**, 69090I (2008).
- ⁴⁶L. A. Dunbar, R. Houdré, G. Scalari, L. Sirigu, M. Giovannini, and J. Faist, *Appl. Phys. Lett.* **90**, 141114 (2007).